Tissue Eng Regen Med (2019) 16(4):415–429
https://doi.org/10.1007/s13770-019-00192-0

Online ISSN 2212-5469

ORIGINAL ARTICLE

Three-dimensional Printed Mg-Doped β-TCP Bone Tissue Engineering Scaffolds: Effects of Magnesium Ion Concentration on Osteogenesis and Angiogenesis *In Vitro*

Yifan Gu[1,2] · Jing Zhang[3,4] · Xinzhi Zhang[4] · Guiping Liang[1,2] · Tao Xu[4,5,6] · Wei Niu[1,2]

Received: 17 January 2019 / Revised: 7 April 2019 / Accepted: 17 April 2019 / Published online: 17 June 2019

Abstract

BACKGROUND: Three-dimensional (3D) printed bone tissue engineering scaffolds have been widely used in research and clinical applications. β-TCP is a biomaterial commonly used in bone tissue engineering to treat bone defects, and its multifunctionality can be achieved by co-doping different metal ions. Magnesium doping in biomaterials has been shown to alter physicochemical properties of cells and enhance osteogenesis.

METHODS: A series of Mg-doped TCP scaffolds were manufactured by using cryogenic 3D printing technology and sintering. The characteristics of the porous scaffolds, such as microstructure, chemical composition, mechanical properties, apparent porosity, etc., were examined. To further study the role of magnesium ions in simultaneously inducing osteogenesis and angiogenesis, human bone marrow mesenchymal stem cells (hBMSCs) and human umblical vein endothelial cells (HUVECs) were cultured in scaffold extracts to investigate cell proliferation, viability, and expression of osteogenic and angiogenic genes.

RESULTS: The results showed that Mg-doped TCP scaffolds have the advantages of precise design, interconnected porous structure, and similar compressive strength to natural cancellous bone. hBMSCs and HUVECs exhibit high proliferation rate, cell morphology and viability in a certain amount of Mg^{2+}. In addition, this concentration of magnesium can also increase the expression levels of osteogenic and angiogenic biomarkers.

CONCLUSION: A certain concentration of magnesium ions plays an important role in new bone regeneration and reconstruction. It can be used as a simple and effective method to enhance the osteogenesis and angiogenesis of bioceramic scaffolds, and support the development of biomaterials and bone tissue engineering scaffolds.

Keywords 3D porous scaffolds · Ion doping · Magnesium ions · Osteogenesis · Angiogenesis

Yifan Gu and Jing Zhang contributed equally to this work.

✉ Tao Xu
taoxu@mail.tsinghua.edu.cn

✉ Wei Niu
niuwei@139.com

[1] The Second Clinical Medical College of Guangzhou University of Chinese Medicine, 232 Waihuan East Road, Guangzhou 510006, China

[2] Orthopedics Department, The Second Affiliated Hospital of Guangzhou University of Chinese Medicine, 111 Dade Road, Guangzhou 510120, China

[3] Medprin Regenerative Medical Technologies Co., Ltd, Guangzhou 510663, China

[4] East China Institute of Digital Medical Engineering, Shangrao 334000, China

[5] Department of Mechanical Engineering, Biomanufacturing Center, Tsinghua University, Beijing 100084, China

[6] Department of Precision Medicine and Healthcare, Tsinghua-Berkeley Shenzhen Institute, Shenzhen 518055, China

1 Introduction

Autografts are considered the "gold standard" for repairing bone tissue due to their high osteoinductive and osteoconductive properties [1, 2]. Usually, autologous bone is taken from healthy tissue (e.g. ilium, tibia or calcaneus) of the patient and re-implanted into the bone defect area. The disadvantage is that the bone mass is limited and cannot meet the needs of large bone defects. Prolonging the operation time also increases the risk of surgical accidents [3, 4]. Allografts are effective substitutes for autografts from tissues obtained from human cadavers and donors. However, there may be risks of immune rejection, low biological activity and pathogen transmission [5]. Although autologous or allogeneic bone grafting has been widely accepted for centuries as a treatment for bone defects, the recovery of large bone defects remains a clinical challenge [6]. The development of bone tissue engineering techniques has attracted great interest in artificial bone tissue scaffolds. In order to be an ideal substitute for bone implants, scaffolds must meet several requirements.

The biomaterial used to prepare the scaffold must have excellent biocompatibility and appropriate biodegradability, which is essential for cell adhesion, proliferation, differentiation, and extracellular matrix formation [7]. β-TCP has been proved to have good biocompatibility, and its composition is similar to natural bone mineral components [8]. In addition, the biodegradation of β-TCP (solubility product, $Ksp = 1.25 \times 10^{-29}$) is much better than other popular bioceramics, such as hydroxyapatite ($Ksp = 2.35 \times 10^{-29}$), which is more advantageous in fitting the bone reconstruction cycle [9]. *In vivo*, they can be degraded and absorbed by the dissolution of body fluids and phagocytosis of cells. The degradation products are calcium and phosphorus ions [10], which can enter the circulatory system and become the basic material for the formation of new bones.

It is also important for the scaffold to have sufficient interconnected porous structure to provide adequate space for biofixation between the scaffold and the reconstructed tissue. Conventional methods for preparing porous scaffolds, such as gas foaming, solvent casting, melt casting, and lyophilization, are difficult to control interconnects, pore size, and total porosity. Depending on the pre-designed shape, three-dimensional (3D) printing can produce a porous scaffold that precisely controls the pore size and interconnects [11]. It has become a key manufacturing technology in bone tissue engineering and has been widely used in pre-clinical or clinical applications [12]. Recent studies have shown that 3D printed TCP scaffolds exhibit efficient bone repair in different bone defect models, such as femoral osteonecrosis [13], mandibular tumor [14], distal femoral defect [15], and calvarial defect [16].

The third requirement is excellent osteoinduction and vascularization. Osteoinduction, which is generally defined as the ability to induce differentiation of osteogenic precursor cells into mature bone cells or more simply, the ability to induce osteogenesis [17]. Substantial studies adopted the addition of functional ions to enhance the osteoinduction of calcium phosphate. Magnesium (Mg) is one of the most abundant ion in biological hard tissue, with concentration around 0.6 (wt%) [18]. It has been reported that magnesium ions (Mg^{2+}) have an effect on bone metabolism, promoting new bone formation and inducing a significant increase in osteogenic activity [19, 20], and they also play a direct and important role in maintaining vascular function [21, 22].

Another requirement is good mechanical performance, ensuring that scaffold can withstand sufficient pressure during surgery and recovery. High-temperature sintering not only removes organic binders (such as cellulose, hydrogels) from bio-inks, but also allows the materials to bond more tightly, increasing the mechanical strength [8, 23, 24]. Ion substitution can also occur during sintering, such as replacement of a portion of Ca^{2+} with Mg^{2+}, which can alter the mechanical and biological properties of the material [25–27].

There is no relevant research report on the effects of Mg^{2+} concentration on mechanical and biological properties of porous TCP scaffolds. Our hypothesis is that properties of porous TCP scaffolds can be improved by 3D printing techniques, high temperature sintering and appropriate concentration of Mg^{2+} doping. To confirm this hypothesis, a series of Mg-doped β-TCP (Mg-TCP) scaffolds were prepared by 3D printing and sintering. The physicochemical properties of the scaffold are characterized by porosity, surface microstructure and phase analysis. The mechanical properties of the scaffold are characterized by compressive strength. In order to study the effect of Mg^{2+} concentration on cellular behavior during bone remodeling, we tested both human bone marrow mesenchymal stem cells (hBMSCs) and human umbilical vein endothelial cells (HUVECs). The effects of a range of magnesium ion concentrations in real-time extracts of Mg-TCP porous scaffolds on cell proliferation, viability and gene expression levels of osteogenic and angiogenic related genes were analyzed.

2 Materials and methods

2.1 Materials

$CaHPO_4 \cdot 2H_2O$, $CaCO_3$, MgO, gelatin and absolute ethanol were purchased from Shanghai Aladdin Bio-Chem Technology Co., Shanghai, China. Cell and cell-associated

complete culture media were supplied by Cyagen Biosciences Inc, Santa Clara, CA, USA. Reagents for cell experiments will be described later. All the commercial chemicals are analytically pure.

2.2 Fabrication and evaluation of Mg-TCP scaffold

2.2.1 Preparation of Mg-TCP powder

The β-TCP powder was synthesized by a high-temperature solid phase reaction method using calcium hydrogen phosphate dihydrate ($CaHPO_4{\cdot}2H_2O$) and calcium carbonate ($CaCO_3$) [28]. Briefly, $CaCO_3$ and $CaHPO_4{\cdot}2H_2O$ powders were mixed at Ca/P = 1.5, and absolute ethanol was added as a wet milling medium to obtain a reaction slurry. After being ball-milled at 300 rpm for 2 h, the material was placed in a blast drying oven to be sufficiently dried. The muffle furnace was used to heat the mixed dry powder gradient to 1000 °C to obtain β-TCP. The chemical reaction equation is shown in Eq. (1):

$$2CaHPO_4 \cdot 2H_2O + CaCO_3 = Ca_3(PO_4)_2 + 5H_2O + CO_2 \uparrow \quad (1)$$

The Mg-TCP formula used in the present study was a mixture of β-TCP and MgO powders at various ratios. Four groups of Mg-TCP powders were prepared with MgO of 0, 1, 2, and 4 wt% (labeled as 0Mg-TCP, 1Mg-TCP, 2Mg-TCP, 4Mg-TCP), and 0Mg-TCP (β-TCP) as the control.

2.2.2 Fabrication of scaffolds through cryogenic 3D printing and sintering

To prepare the Mg-TCP bio ink, 4 g of Mg-TCP powder and 2 mL 20 wt% gelatin solution were added to a 10 mL beaker. The powder–gel mixture was thoroughly stirred with a glass rod until it looked like a toothpaste. The printing procedure is shown in Fig. 1. Briefly, the pre-designed print pattern was sliced and converted to a gcode file by Slic3r (free access, Alessandro Ranellucci). These gcode files were then sent to the 3D printer (Livprint Norm, Medprin, Guangzhou, China). The powder-gel mixture was loaded into a special 3 ml syringe, and a printing nozzle having an inner diameter of 420 μm (22 gauge) was used in consideration of a suitable filament diameter and pore diameter. The temperature of the platform was set to − 5 °C to ensure rapid solidification. After all the printed scaffolds were freeze-dried for 48 h, they were sintered at 1250° for 2 h in a muffle furnace to remove the organic binder.

2.2.3 Scaffolds characterization

Four groups of Mg-TCP scaffolds were crushed and ground into powders. The powdered scaffolds were analyzed by an X-ray diffractometer (XRD; X'Pert PRO, PANalytical Co., Almelo, The Netherlands) using CuKα radiation (λ = 1.5418 Å, 40 kV, 40 mA). Data were collected for 2θ

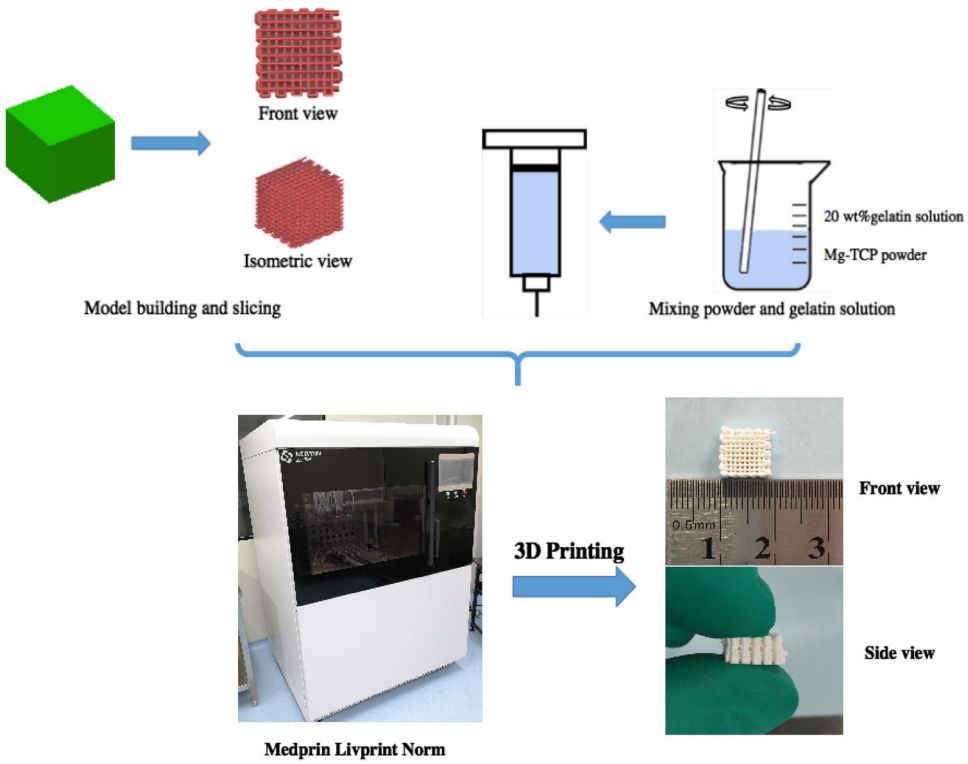

Fig. 1 3D printing and sintering process for Mg-TCP porous scaffolds

from 10° to 80° with a step size of 0.0166° and estimated by Jade software (version 6.5) with standard reference intensity ratio (RIR) [29].

The morphology of scaffolds was observed by a field emission scanning electron microscope (SEM; ULTRA 55, LEO Gemini, Zeiss, Oberkochen, Germany) equipped with an energy dispersive X-ray spectrometer (EDS; XFlash 6130, Bruker, Karlsruhe, Germany). Before SEM observation, all samples were mounted on an aluminum stub by carbon tape and coated with a thin layer of gold. Accelerating voltages of 15 kV were used.

The compressive strength of Mg-TCP scaffolds samples (10 mm × 10 mm × 8 mm) were measured using a universal material testing machine (Model E34, Exceed, MTS, Eden Prairie, MN, USA) at a crosshead speed of 0.5 mm/min.

Based on the Archimedes' principle, the apparent porosity of the scaffolds is determined by hydrostatic weighing. The real volume (labeled as V_1) of the scaffolds was calculated with Eq. (2):

$$V_1 = (W_0 + W_1 - W_2)/\rho_{water} \quad (2)$$

where ρ_{water} is the density of water (0.99705 g/cm^3) at 25°, W_0 (g) is the weight of a pycnometer filled with deionized water, W_1 (g) is the weight of each scaffold. The scaffold was then immersed in a pycnometer and filled with deionized water by vacuum. After that, the entire pycnometer was filled again, weighed and labeled as W_2 (g). The apparent porosity of the scaffolds was determined according to Eq. (3):

$$\text{Porosity}(\%) = (V_0 - V_1)/V_0 \times 100\% \quad (3)$$

where V_0 (cm^3) is the apparent volume of scaffolds, calculated by the length, width and height of the scaffolds.

2.3 *In vitro* cell experiment of Mg-TCP

2.3.1 Preparation of Mg-TCP extracts

Mg-TCP scaffolds were sterilized by ^{60}Co γ-irradiation at 20 kGy, and then respectively added into complete culture mediums of hBMSCs and HUVECs at a weight-to-medium volume ratio of 0.1 g/mL. A real-time extraction at 37 °C was performed. Namely, the soaking solutions of scaffolds were completely gathered under sterile conditions and fresh complete culture mediums were reused every other day to produce the real-time Mg-TCP extracts.

2.3.2 Release behavior of ions in scaffolds extracts

Fresh and spent real-time Mg-TCP extracts were collected and then digested with concentrated nitric acid at 90° for 10 min. Inductively coupled plasma atomic emission spectrometry (ICP-AES; Optima 5300DV, Perkin Elmer, Waltham, MA, USA) was used to determine the concentrations of Mg, Ca and P in digested extracts in order to study the ion release behavior of Mg-TCP porous scaffolds. At each time point, the detection volume of each sample was 5 ml, and three parallel samples were set for each group. The results of ICP-AES were compared to analyze the changes of cellular behavior induced by magnesium ion concentration.

2.3.3 Cell culture

Human bone marrow mesenchymal stem cells (hBMSCs; No. HUXMA-01001, Cyagen, Santa Clara, CA, USA) and human umbilical vein endothelial cells (HUVECs; No. HUVECs-20001, Cyagen, Santa Clara, CA, USA) were used to study the effects of Mg^{2+} on cell proliferation, viability, osteogenesis and angiogenesis. The hBMSCs and HUVECs were cultured in cell culture flasks in an incubator (37 °C, 5% CO_2) with a humidified atmosphere. Complete media (for hBMSCs: No. HUXMA-90011, Cyagen, Santa Clara, CA, USA; for HUVECs: No. HUVECs-90011, Cyagen, Santa Clara, CA, USA) were used for cell culture and were refreshed every other day. Cells at passage 5 were used for the following experiments.

2.3.4 Cell proliferation

The proliferation of hBMSCs and HUVECs was evaluated using a Cell Counting Kit-8 (CCK-8; Dojindo, Kumamoto, Japan), following the manufacturer's instructions. Cells that were seeded on 48-well plates (1×10^4 cells per well) were cultivated in the incubator for 1, 4 and 7 days and the extracts were exchanged every other day. At each time point, the CCK-OD was read at 450 nm by using an enzyme-labeled instrument (Epoch 2, BioTek, Winooski, VT, USA). A calibration curve with cell number and absorbance was created to convert the detected optical density (OD) to the number of cells.

2.3.5 Cell viability assay

A fluorescent live/dead assay kit (calcein-AM; No. KGAF001, KeyGEN BioTECH, Nanjing, China) was used to stain cells for the cell viability study. Briefly, after the cells (2×10^4 cells per well) were cultured with extracts for 24 h, the cells on plates were rinsed three time with PBS and incubated with calcein-AM working solution (containing 8 μM propidium iodide and 2 μM calcein AM) in a humidified incubator (37 °C, 5% CO_2) for 45 min. Subsequently, the result was observed by fluorescence microscopy (Eclipse Ti2-U, Nikon, Tokyo, Japan). Live cells presented in green while dead cells were red.

2.3.6 Immunofluorescence staining of cytoskeletons

After 24 h of cultivation, nuclear and F-actin staining was performed on hBMSCs and HUVECs cultured in different groups of Mg-TCP extracts. The cells were first fixed with 4% paraformaldehyde solution. After washing with PBS, the cells were permeabilized in 0.1% Triton X-100 solution. Washing again with PBS, phalloidin-iFluor 488 conjugate (No. 23115, AAT Bioquest Inc, Sunnyvale, CA, USA) was added to the cells for F-actin staining and incubated at 37° for 1 h. With another washing, the 4′,6-diamidino-2-phenylindole (DAPI; No. C0065, Solarbio Life Sciences, Beijing, China) solution was added to the samples for nuclear staining and incubated at room temperature for 10 min. Fluorescent images were observed under an inverted fluorescence microscope (Eclipse Ti2-U, Nikon, Tokyo, Japan) and analyzed using Image J software (National Institutes of Health, Bethesda, MD, USA).

2.3.7 Alkaline phosphatase (ALP) staining and activity assay

The ALP activity of hBMSCs cultured in Mg-TCP extracts was measured with an alkaline phosphatase activity test kit (No. 70-AP0011, MultiSciences, Hangzhou, China), which was based on transformation from p-nitrophenyl phosphateto (pNPP) to p-nitrophenyl (pNP) in the presence of ALP. The cells at a concentration of 3×10^4 cells/well were cultured in 500 μL of Mg-TCP extracts (added 10 mM β-glycerophosphate, 10 nM dexamethasone and 50 mg/mL vitamin C) in 48-well plates. ALP activity assays were performed on days 7, 10 and 14, following the manufacturer's instructions. The optical density was read at 405 nm.

ALP staining was performed after 7, 10 and 14 days of cell culture by using BCIP/NBT substrate solution (No. C3206, Beyotime Biotechnology, Shanghai, China). Briefly, cells were washed three times with PBS and fixed with 4% paraformaldehyde solution for 1 h. Then, the residual paraformaldehyde was washed off with PBS and 150 μL ALP staining working solution was added into each well. After half an hour of staining, PBS washing was performed to remove the residual ALP staining working solution. The purple product was observed by the inverted fluorescence microscope and analyzed using Image J software.

2.3.8 Alizarin red S (ARS) assay

The extracellular matrix mineralization was qualitatively assessed by Alizarin red S (ARS, No. S0141, Cyagen, Santa Clara, CA, USA) assay. ARS stained the calcium nodules after hBMSCs were cultured in extracts for 14 days and 21 days. The cells were fixed with 4% paraformaldehyde solution for 1 h, washed three times with deionized water, and then stained with ARS solution for 10 min. The residual ARS stain was washed with deionized water. The image was taken by the inverted fluorescence microscope and analyzed using Image J software.

2.3.9 Nitric oxide (NO) staining assay

The endothelium-derived NO generated by HUVECs was detected by NO staining with diaminofluorescein-FM diacetate (DAF-FM DA, 5 mM; No. KGA515, KeyGEN BioTECH, Nanjing, China). A working solution of 5 μM DAF-FM DA was achieved by dissolving DAF-FM DA in basal medium (without serum and phenol red) according to the instructions. Cells (1×10^5 cells per well) were cultured with the Mg-TCP extracts in 6-well plates for 48 h. Then the cells were incubated in DAF-FM DA working solution for 20 min at 37 °C. The fluorescent images were recorded with the inverted fluorescence microscope, and the fluorescence intensity of each group after DAF-FM DA probe labeling was also analyzed by flow cytometry (CytoFLEX, Beckman Coulter, Brea, CA, USA).

2.3.10 Quantitative real time PCR assay

Gene expression levels of runt-related transcription factor 2 (Runx-2), collagen type I (Col-I), osteocalcin (OCN), alkaline phosphatase (ALP) and bone sialoprotein (BSP) in hBMSCs and gene expression levels of vascular endothelial growth factor (VEGF) and endothelial nitric oxide synthase (eNOS) in HUVECs were detected by quantitative real-time polymerase chain reaction (qPCR). The cells (1×10^5 cells per well in 6-well plates) were cultured in the extracts for 7 days and 14 days, total RNA in cells was isolated by using Trizol (No. R0016, Beyotime Biotechnology, Shanghai, China) according to the manufacturer's protocol. Reverse transcription was performed using the cDNA Synthesis Kit (with gDNA Eraser; No. D7170 M, BeyoRT™ II, Beyotime Biotechnology, Shanghai, China). DNA transcription was carried out using SYBR Green qPCR Mix (2X; No. D7260, BeyoFast™, Beyotime Biotechnology, China). The qPCR analysis was performed using qTOWER3 (Analytik Jena AG, Jena, Germany) and GAPDH was treated as a housekeeping gene. The primer sequences [30] are listed in Table 1. Relative gene expression was calculated using the $2^{-\Delta Ct}$ method. Experiments were performed in triplicate to obtain the final mean value and standard deviation.

2.4 Statistical analysis

All statistical analyses were performed using StataSE software (version 14). The results are presented as mean

Table 1 The primer sequences for qPCR assay

Target gene	Forward primer sequences (5′–3′)	Reverse primer sequences (3′–5′)
GAPDH	AGAAAAACCTGCCAAATATGATGAC	TGGGTGTCGCTGTTGAAGTC
Runx-2	AGATGATGACACTGCCACCTCTG	GGGATGAAATGCTTGGGAACT
Collagen-I	CAGCCGCTTCACCTACAGC	TTTTGTATTCAATCACTGTCTTGCC
OCN	TCACACTCCTCGCCCTATTG	ACAGTCCGGATTGAGCTCAC
ALP	ACATTCCCACGTCTTCACATTT	AGACATTCTCTCGTTCACCGCC
BSP	ATGGCCTGTGCTTTCTCAATG	GGATAAAAGTAGGCATGCTTG
VEGF	TGCGGATCAAACCTCACCA	CAGGGATTTTTCTTGTCTTGCT
eNOS	TGTCCAACATGCTGCTGGAAATTG	AGGAGGTCTTCTTCCTGGTGATGCC

value ± standard deviation. Comparative studies of mean values were analyzed using one-way analysis of variance (ANOVA) with the student's t test. $P < 0.05$ was considered statistically significant. All data were presented using GraphPad Prism 7 software.

3 Results

3.1 Physicochemical properties of Mg-TCP scaffold

The XRD patterns of the Mg-TCP scaffold powder (Fig. 2) show that β-TCP [$Ca_3(PO_4)_2$; PDF#70-2065] and hydroxyapatite ($Ca_{10}(PO_4)_6(OH)_2$; PDF #74-0566) were the major crystal form of all groups. In addition, α-TCP ($Ca_3(PO_4)_2$; PDF#29-0359) were produced in 0Mg-TCP. Interestingly, a new crystal, calcium magnesium phosphate [$Ca_{2.86}Mg_{0.14}(PO_4)_2$; PDF#70-0681], was formed in the MgO doped groups.

The 3D printed Mg-TCP scaffolds showed the same porous surface structure as the designed CAD model. Under the electron microscope, the four groups of scaffolds showed similar structures (Fig. 3A, B, the SEM images of 0Mg-TCP, 2Mg-TCP and 4Mg-TCP are not displayed here). The front pores are approximately square, the length is 400 μm. And the side pores are approximately rectangular, the size is 300 μm × 100 μm. EDS mapping analysis of 0Mg-TCP, 1Mg-TCP and 2Mg-TCP showed that the Ca, Mg and P elements in the scaffold fibers were evenly distributed (Fig. 3C–E). However, the Mg element condenses in 4Mg-TCP, which may be caused by uneven mixing of bio-ink (Fig. 3F).

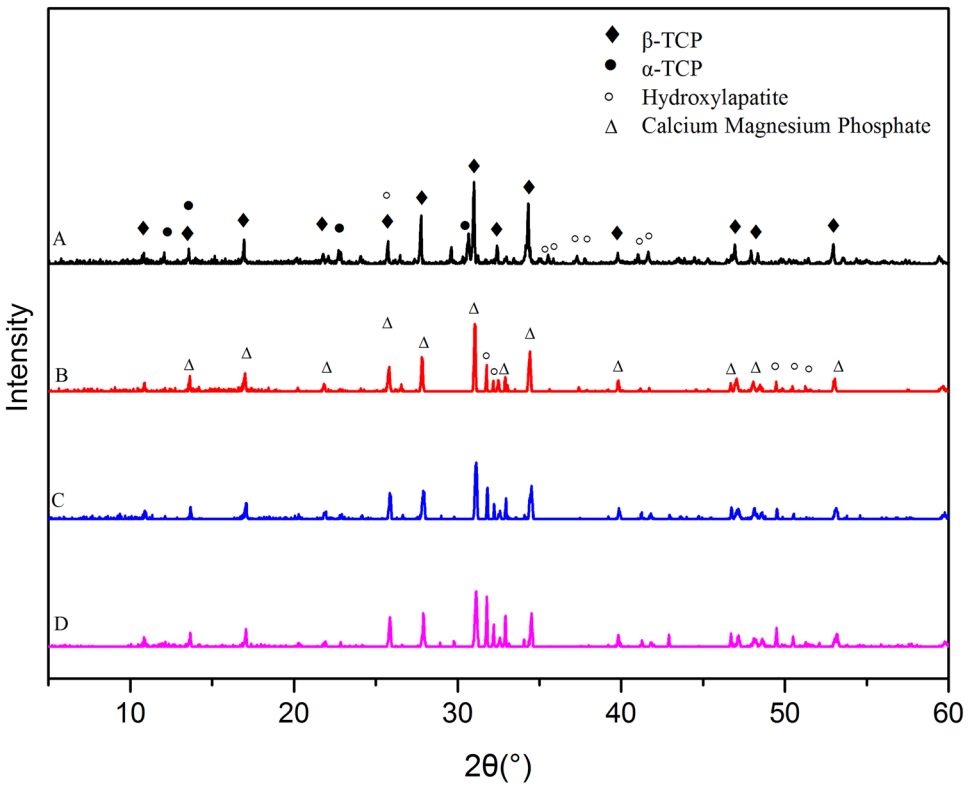

Fig. 2 X-ray diffraction pattern of each group of Mg-TCP porous scaffolds

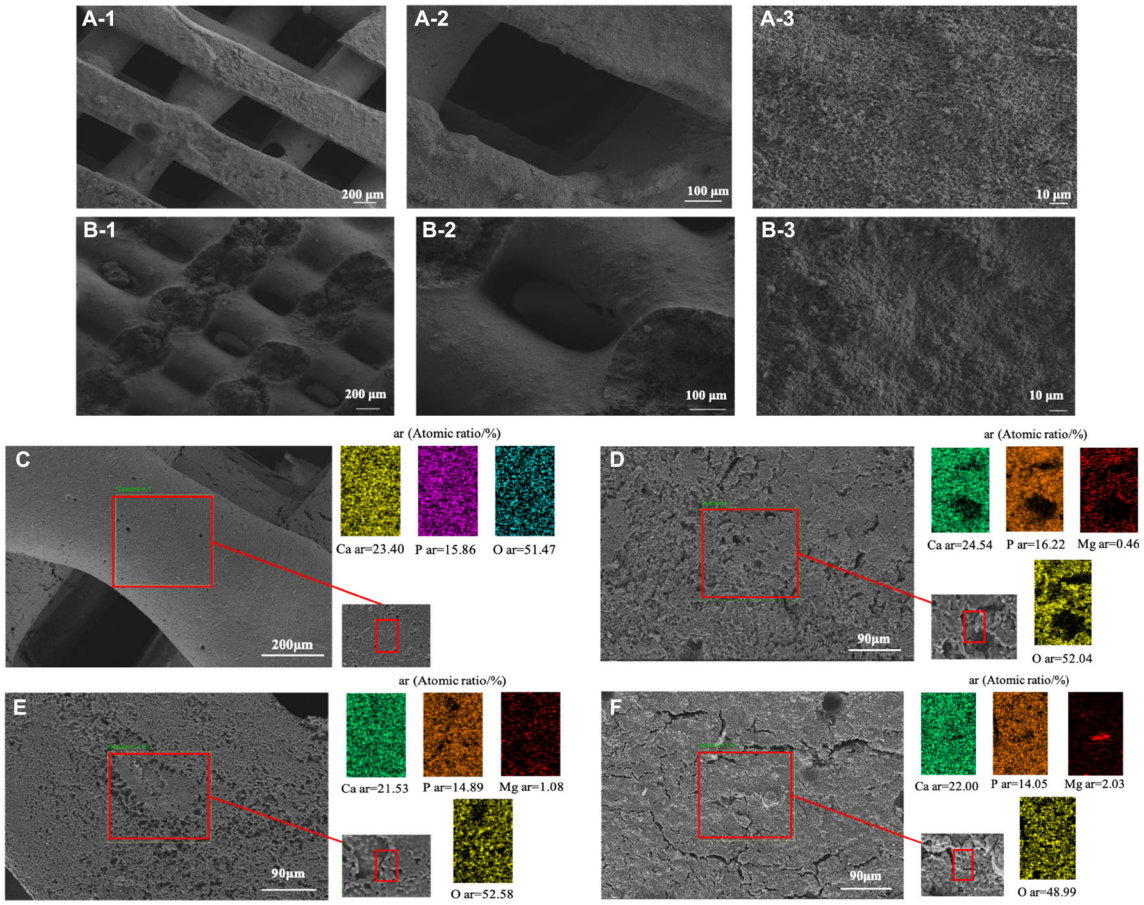

Fig. 3 SEM images of front view (A1–A3) and side view (B1–B3) of 1Mg-TCP porous scaffolds. EDS analysis of the elemental distribution of Mg-TCP (C:0Mg-TCP, D: 1Mg-TCP, E: 2Mg-TCP, F: 4Mg-TCP)

The mechanical properties test results of the scaffolds are shown in Table 2. Magnesium doping can improve the mechanical properties of the porous scaffold. The maximum load pressure that the magnesium-doped scaffold can withstand is more than three times higher than that of the TCP (0Mg-TCP) scaffold. It can be seen that 1Mg-TCP has the best mechanical properties ($*p < 0.01$).

The apparent porosity of the porous scaffold is shown in Table 3. The porosity of all scaffolds was between 60% and 70%, and there was no significant difference in apparent porosity between the different groups ($*p > 0.05$).

Table 2 The compressive strength of scaffolds

Group	Maximum load stress (MPa)	Young's modulus (MPa)
0Mg-TCP	8.45 ± 0.77	230.25 ± 68.57
1Mg-TCP	30.69 ± 3.90	930.65 ± 163.79*
2Mg-TCP	27.01 ± 1.24	565.78 ± 139.04
4Mg-TCP	26.58 ± 2.43	549.13 ± 84.77

3.2 Release behavior of ions in Mg-TCP extracts

Figure 4 showed the changes in Ca, Mg and P concentrations of the Mg-TCP scaffold extracts for 14 days. The concentration of Ca^{2+} in the extract did not change significantly with time, while the concentration of P ions showed an upward trend in the extract. The concentration of Mg^{2+} released from each group was positively correlated with the ratio of magnesium. Since 0Mg-TCP does not contain magnesium, the detected Mg ions were from the medium. As the soaking time increased, the concentration of Mg^{2+} gradually reduced. Figure 4A showed the concentration of Mg^{2+} at different time points in fresh extracts. On the first day, the concentration of Mg^{2+} in

Table 3 The apparent porosity of scaffolds

Group	Apparent porosity
0Mg-TCP	61.35% ± 4.40%
1Mg-TCP	62.22% ± 5.44%
2Mg-TCP	62.97% ± 5.53%
4Mg-TCP	64.32% ± 6.41%

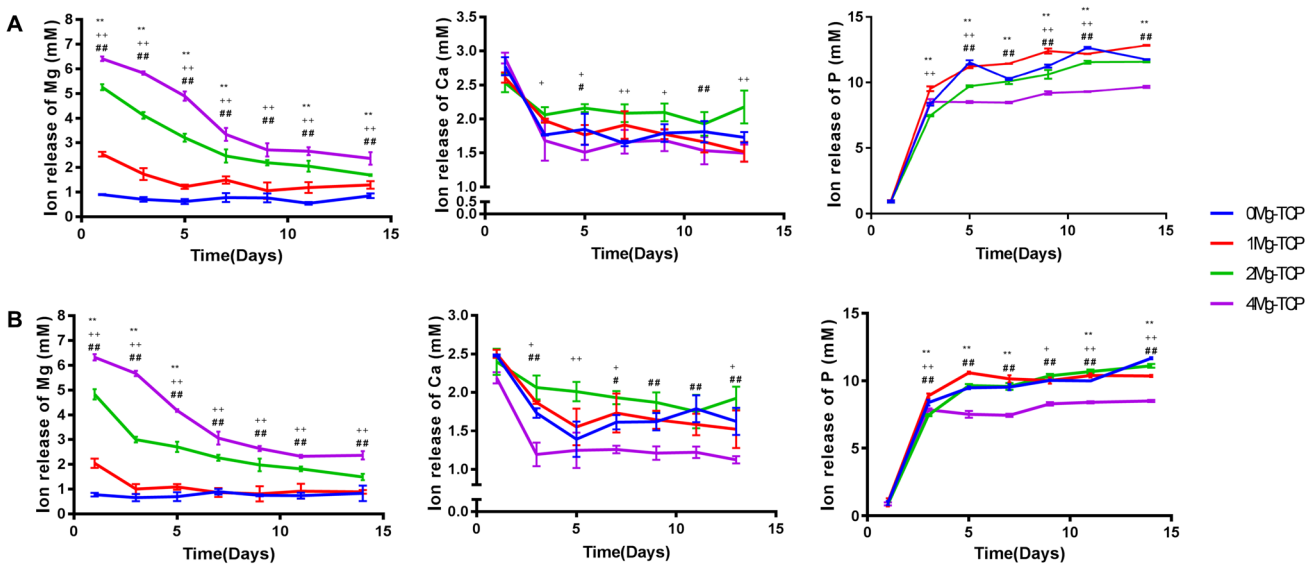

Fig. 4 Release of Ca and Mg ions in four groups of Mg-TCP porous scaffolds in complete medium: **A** ion concentration in the extract before culturing the cells, **B** ion concentration in the extract after culturing the cells (n = 4; 1Mg-TCP compared with 0Mg-TCP, $*p < 0.05$ and $**p < 0.01$; 2Mg-TCP compared with 0Mg-TCP, $+p < 0.05$ and $++p < 0.01$; 4Mg-TCP compared with 0Mg-TCP, $\#p < 0.05$ and $\#\#p < 0.01$)

1Mg-TCP was 2.31 ± 0.12 mM, in 2Mg-TCP was 5.25 ± 0.11 mM, and in 4Mg-TCP was 6.46 ± 0.19 mM. On the 14th day, the Mg^{2+} concentration in 1Mg-TCP reduced to 0.96 ± 0.20 mM, 2Mg-TCP to 1.66 ± 0.12 mM, and 4Mg-TCP to 2.38 ± 0.18 mM. Figure 4B showed the concentration of ion in the extract after culturing the cells. It is worth noting that in general, the concentration of Ca^{2+} and Mg^{2+} decreased in the extract after cell culturing. On day 1, the concentration of Mg^{2+} in 1Mg-TCP was 1.94 ± 0.18 mM, in 2Mg-TCP was 4.90 ± 0.15 mM, and in 4Mg-TCP was 6.35 ± 0.19 mM. On the last day, the Mg^{2+} concentration in 1Mg-TCP was 0.87 ± 0.15 mM, in 2Mg-TCP was 1.63 ± 0.19 mM, and in 4Mg-TCP was 2.14 ± 0.18 mM. This phenomenon may indicate that Ca^{2+} and Mg^{2+} in the Mg-TCP extract were involved in cellular metabolism and participated in changes in cellular behavior.

3.3 Viability, morphology and proliferation of hBMSCs and HUVECs

Proliferation assays in current studies showed concentration-dependent cellular behavior. As the culture time was prolonged, the cell number of hBMSCs increased, and the cells cultured in 1Mg-TCP extract proliferated best (Fig. 5A). HUVECs cultured in 0Mg-TCP and 1Mg-TCP extracts showed an increase in proliferation at each time point, and proliferation in 1Mg-TCP extract was higher than that in 0Mg-TCP. However, the number of cells cultured in 2Mg-TCP extract on the 4th day and the 7th day did not change significantly, and the cells cultured in 4Mg-TCP extract showed inhibition of proliferation (Fig. 6).

The activity of hBMSCs (Fig. 5B) and HUVECs (Fig. 6B) in different extracts showed that cells stimulated by four groups of Mg-TCP extracts remained viable. Only a small amount of cells died in each sample, which presented as red spots on the image.

Cytoskeletal proteins play a crucial role in cell migration and cell morphology support. The incorporation of Mg^{2+} in this experiment allowed hBMSCs (Fig. 5C) and HUVECs (Fig. 6C) in the extracts to have a diffusion morphology and cytoskeletal protein production. The cellular area of hBMSCs and HUVECs cultured in 1Mg-TCP extracts was significantly larger than that of the other three groups. The results indicate that 1Mg-TCP could better promote cell migration and spreading.

3.4 Effect of sustained release of Mg^{2+} on the osteogenic induction of hBMSCs

ALP activity increased during the assay and peaked in all four groups treated with Mg-TCP extracts on day 14. On day 10, the ALP activity of 1Mg-TCP was significantly higher than that of any other group. The 1Mg-TCP group had a constant positive effect on ALP activity and reached its highest level on day 14 (Fig. 7). As shown in Fig. 8, the ALP stained positive area in 1Mg-TCP was significantly larger than that in the other three groups on the day 10 of induction culture, which was consistent with the quantitative analysis of ALP activity.

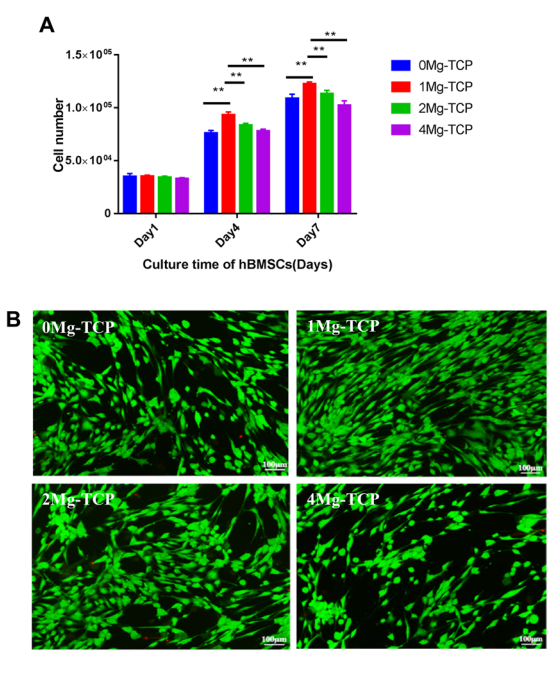

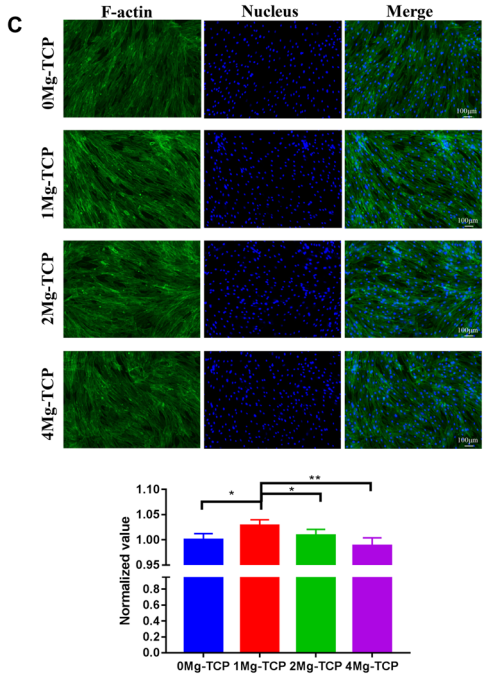

Fig. 5 **A** Influence of a series of Mg-TCP extracts on the proliferation of hBMSCs after being cultured for 1, 4 and 7 days, quantified using CCK-8 assay (detection at 450 nm); **B** live/dead fluorescence photographs of hBMSCs after being cultured in Mg-TCP extracts for 24 h; **C** cytoskeleton and nucleus fluorescence photographs of hBMSCs after being cultured in Mg-TCP extracts for 24 h and quantitative analysis data for cellular area of hBMSCs. (n = 4; $*p < 0.05$, $**p < 0.01$)

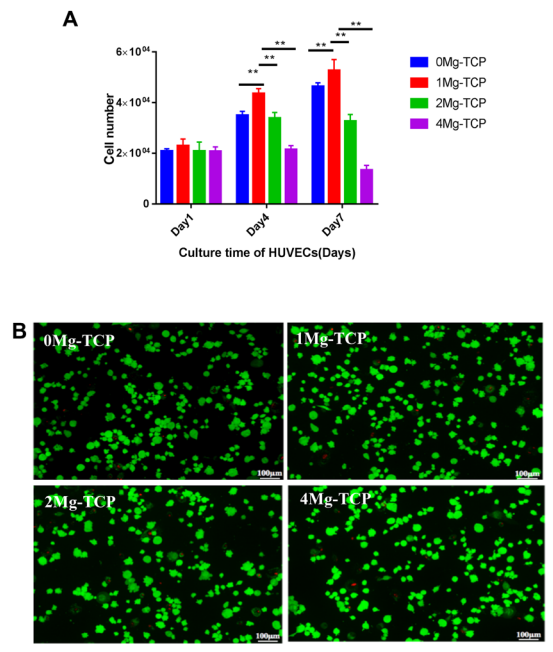

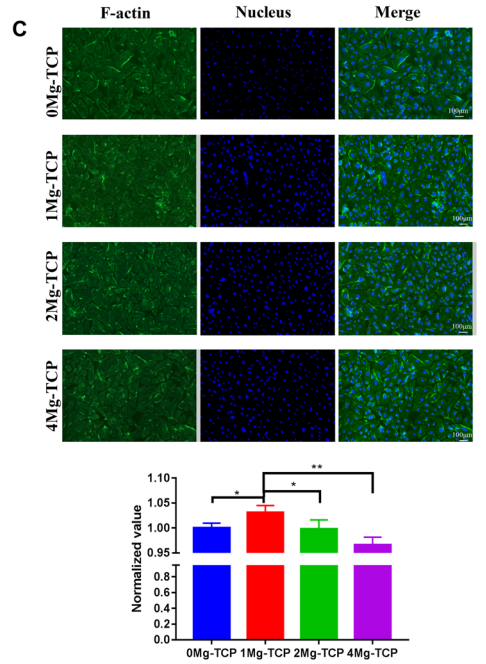

Fig. 6 **A** Influence of a series of Mg-TCP extracts on the proliferation of HUVECs after being cultured for 1, 4 and 7 days using CCK-8 assay (detection at 450 nm); **B** live/dead fluorescence photographs of HUVECs after being cultured in Mg-TCP extracts for 24 h; **C** cytoskeleton and nucleus fluorescence photographs of HUVECs after being cultured in Mg-TCP extracts for 24 h and quantitative analysis data for cellular area of HUVECs. (n = 4; $*p < 0.05$, $**p < 0.01$)

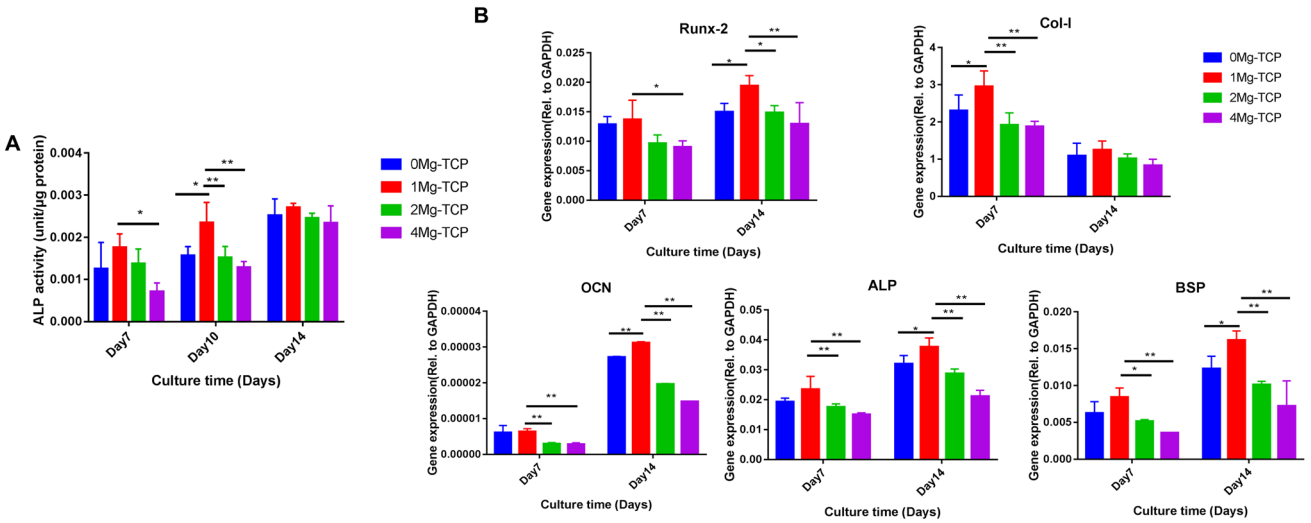

Fig. 7 **A** ALP activity of hBMSCs cultured in 0Mg-TCP, 1Mg-TCP, 2Mg-TCP and 4Mg-TCP extract for 7, 10 and 14 days (n = 4; $*p < 0.05$, $**p < 0.01$). **B** The osteogenesis-related gene expression levels of Runx-2, Col-I, OCN, ALP and BSP after 7 days and 14 days of hBMSCs culture in Mg-TCP extracts (n = 6; $*p < 0.05$, $**p < 0.01$)

After 14 days of culture, the image of the ARS assay (Fig. 8B) showed that the 1Mg-TCP extract had more calcium nodules than the other group extracts. The ARS stained positive area in 1Mg-TCP was the largest, indicating that Mg^{2+} concentration of this group had a good induction effect on the mineralization of extracellular matrix.

To evaluate the role of Mg^{2+} in promoting osteogenesis, qPCR was performed on days 7 and 14 of cell culture. We chose Runx2, Col-I, ALP, OCN and BSP, which are considered to be biomarkers of osteogenic differentiation. Expression of Runx-2 promotes the differentiation of hBMSCs into fully mature osteoblasts and bone formation, and is down-regulated with the maturation of osteoblasts [31]. The expression of Col-I and ALP is a marker of osteoblast differentiation. Col-I has the function of forming and maintaining skeletal integrity and plays an important role in maintaining the internal environment and transmitting extracellular signals [32]. Alkaline phosphatase (ALP) is an external enzyme of osteoblasts, it can hydrolyze phosphate during osteogenesis, provide the necessary phosphoric acid for the deposition of hydroxyapatite, and hydrolyze pyrophosphate to alleviate its inhibition of bone salt formation, which is beneficial for bone formation. The expression of bone sialoprotein (BSP) promotes nucleation of hydroxyapatite mineralization and increases calcium binding and nodule formation [33]. The expression of osteocalcin (OCN) is exhibited in late stage osteoblasts, and osteocalcin is closely related to extracellular matrix mineralization. As showed in Fig. 7B, the abundances of osteogenic related transcripts in cells cultured in 1Mg-TCP extract were higher than those in the other three groups.

3.5 Effects of sustained release of Mg^{2+} on angiogenesis in HUVECs

Endothelial cell-derived nitric oxide (NO) is an important factor in the survival of endothelial cells. In this experiment, we confirmed that Mg^{2+} has angiogenic properties by DAF-FM DA fluorescent probe labeling. As showed in Fig. 9A, HUVECs cultured in 1Mg-TCP extract produced the most NO.

Expression of angiogenesis-related genes, including VEGF and eNOS, was detected by qPCR. Vascular endothelial growth factor (VEGF) can promote vascular permeability, extracellular matrix degeneration, vascular endothelial cell migration, proliferation and angiogenesis. Endothelial nitric oxide synthase (eNOS) plays an important role in regulating endothelial function and produces endothelial cell-derived nitric oxide (NO) as a major regulator of vascular tone [34]. The results showed that cells cultured in 1Mg-TCP extract showed the highest levels of angiogenic related gene expression (Fig. 9B).

Further, the results showed that the cells cultured in the Mg-doped TCP scaffold extract, especially the cells cultured in 1Mg-TCP, exhibited higher expression of osteogenesis and angiogenesis related genes.

4 Discussion

4.1 Physicochemical properties of Mg-TCP scaffold

Cryogenic 3D printing technology enables the rapid manufacture of porous supports with individual structures. It has become an attractive manufacturing technique for the

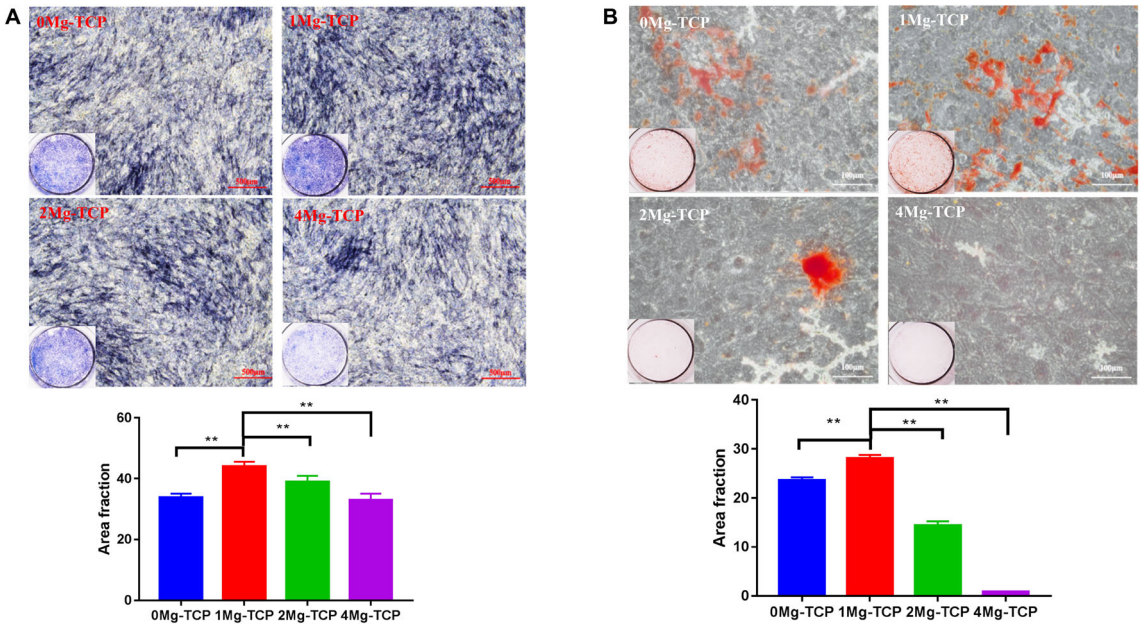

Fig. 8 **A** ALP staining images (stereomicroscope and ×40 magnification microscope) of hBMSCs cultured in Mg-TCP extract for 10 days and quantitative analysis data for positive area. **B** ARS staining images (stereoscope and ×40 magnification microscope) of hBMSCs cultured in Mg-TCP extract for 14 days and quantitative analysis data for positive area. (n = 4; $*p < 0.05$, $**p < 0.01$)

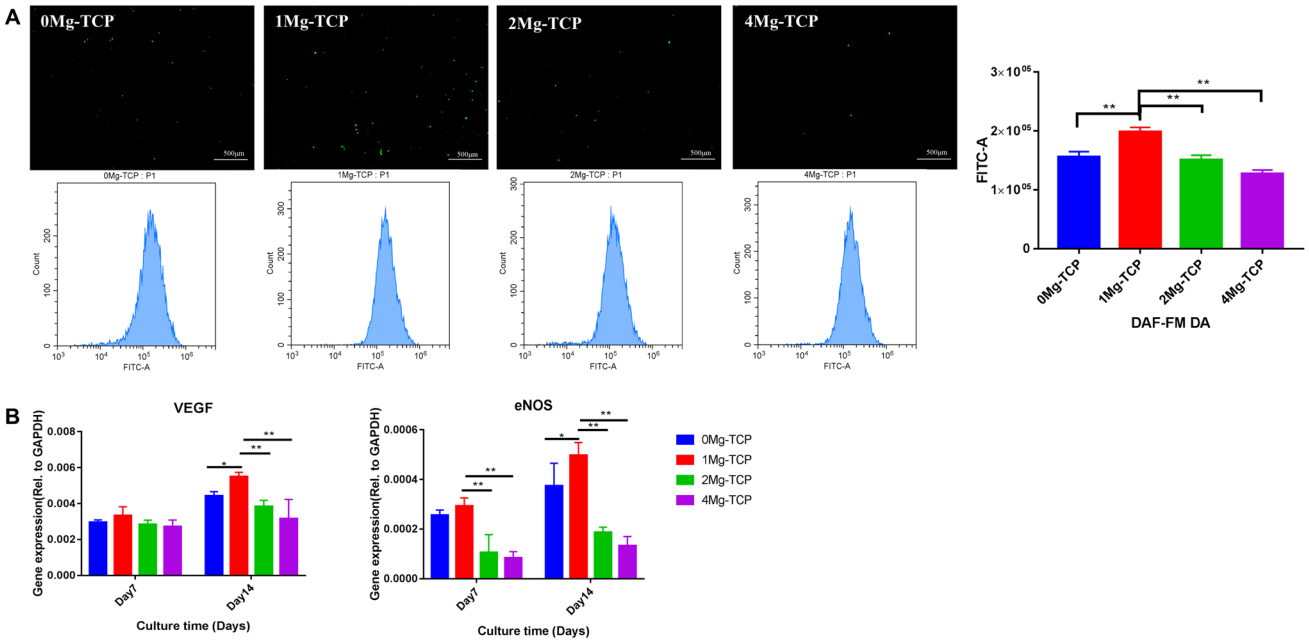

Fig. 9 **A** After 48 h of culture in the four groups of Mg-TCP extracts, the production of NO in HUVECs was detected by DAF-FM DA probe labeling (n = 4; $*p < 0.05$, $**p < 0.01$). **B** The angiogenic-related gene expression levels of VEGF and eNOS after 7 days and 14 days of HUVECs culture in Mg-TCP extracts (n = 6; $*p < 0.05$, $**p < 0.01$)

synthesis of bone tissue engineering scaffolds for research and clinical applications. In this study, we successfully manufactured Mg-doped TCP scaffolds with precisely designed and interconnected porous structures via cryogenic 3D printing technology and high temperature sintering process.

The optimal pore size of 200–600 μm is proposed in the literature to ensure the potential space for cell growth, nutrient diffusion, osteogenesis and angiogenesis [8, 35]. The Mg-TCP scaffolds designed in our study have a pore size of about 400 μm and a filament diameter of 450 μm, which can satisfy cell migration and nutrient exchange, and

provide the necessary mechanical support. It can also be seen from the SEM image that the sintering process only causes slight shrinkage of the scaffold filaments. The porosity of the scaffold was chosen to match the corresponding porosity of the native bone, and the porosity of the cancellous bone was reported to be 50–90% [36]. As described above, the porosity of all four groups of scaffolds is between 60 and 70%, which similar to cancellous bone.

Mechanical properties are another major criterion for porous bone engineering scaffolds. In our study, the compressive strength of all the scaffolds was greater than 3 MPa, which is similar to the compressive strength of human cancellous bone (3–30 MPa) [37]. Products of Mg^{2+} substitution into calcium phosphates during sintering can be an amorphous phase or a crystalline structure, which can cause a series of changes in physical properties [38]. This may be one of the reasons for the significant increase in the compressive strength of Mg-doped TCP. The results of EDS analysis confirmed that magnesium was uniformly distributed on the TCP scaffold. The increase in compressive strength can also be explained by the theory of particle dispersion strengthened ceramics. The specific mechanism of mechanical strength change caused by Mg^{2+} doping remains to be further studied.

As shown in the XRD pattern, partial TCP in the 0Mg-TCP group changed from the β phase to the α phase after sintering. The temperature gradually increases from room temperature to 1250° (5°/min) during the sintering process, including the TCP phase transition temperature (1120°–1170°), which may be the reason for the production of α-TCP. However, no significant α-TCP was observed in MgO doping groups. Frasnelli M et al. found in their study that the presence of magnesium in the TCP lattice promoted spontaneous α → β reconversion during rapid cooling and slowed the β → α transition during heating [39]. Due to the presence of Mg^{2+}, a small part of Ca^{2+} ions in β-TCP crystals were instead, the three Mg-containing groups also produced calcium magnesium phosphate ($Ca_{2.86}Mg_{0.14}(PO_4)_2$), which was a kind of β-TCMP (Mg-substituted beta-tricalcium phosphate) [40].

4.2 Effect of magnesium ion concentration on cellular behavior *in vitro*

Osteogenesis and angiogenesis are both critical for bone scaffolds. The released Mg^{2+} stimulated the behavior of the cells. The role of Mg^{2+} has demonstrated that it significantly enhances the adhesion and spreading of cells, which could improve bone healing [41–43]. Researchers have demonstrated that magnesium ions can regulate the expression of bone-related genes such as Runx2, ALP, OCN and OPN through the PI3 K/Akt signaling pathway [44–46]. Furthermore, Mg-doped calcium phosphate can effectively regulate the adsorption direction of fibronectin (Fn), enhance its receptor binding affinity, and up-regulate the expression of α5β1 in BMSC, which significantly enhances BMSC adhesion and osteogenic differentiation [47]. The bone vasculature also plays a pivotal role in bone growth, remodeling, and homeostasis. Extracellular Mg^{2+} could induce endothelial cell proliferation and migration through G protein coupled receptor pathway during angiogenesis [48]. VEGF and eNOS are the key players in the process of angiogenesis. Mg^{2+} can enter HUVECs through caveolin-1-mediated endocytosis, reduce the level of caveolin-1 and increase the activity of eNOS [49]. In the present study, MgO was selected as the source of Mg^{2+} and complexed with β-TCP. The high temperature of sintering caused the doped MgO to react with part of β-TCP to form β-TCMP. Composites incorporating MgO can take advantages of the potential benefits of MgO while reducing toxicity [50]. Singh et al. reported that β-TCMP enhanced MSC proliferation and differentiation compared to β-TCP [27]. Su et al. described that both calcium phosphate and calcium magnesium phosphate can enhance the angiogenesis potential of HUVEC by activating Akt/eNOS/VEGF pathway, and the effect of calcium magnesium phosphate is stronger than that of calcium phosphate [51].

Our study found that the sustained release of magnesium ions in the 1Mg-TCP porous scaffold has optimal *in vitro* osteogenic and angiogenic induction effects. Previous studies have shown that Mg^{2+} at concentrations below 10 mM did not induce apoptotic cell death in hBMSCs [26]. When applied at a concentration of around 10 mM, Mg^{2+} had no adverse effects but instead improved endothelial cell migration [52]. Fluorescent staining of live/dead cells and cytoskeleton in our study showed that the four groups of Mg-TCP scaffold extracts had no significant acute cytotoxicity and maintained cell morphology integrity at the early stage of cell culture.

It is well known that a suitable concentration of Mg^{2+} enhances the osteogenic activity of BMSCs [50]. As shown in the results, hBMSCs induced in the 1Mg-TCP group (initial Mg^{2+} concentration was 2.31 ± 0.12 mM) were superior to other groups in terms of cell proliferation and osteogenesis-related gene expression. Wong et al. reported that magnesium ions at a concentration of 50 ppm (approximately 2 mM) can significantly promote the proliferation and differentiation of pre-osteoblasts and the up-regulation of osteogenic genes *in vitro* as well as significant new bone formation *in vivo* [53]. However, Mg^{2+} concentration above 5 mM has detrimental effects on human osteoblast differentiation and osseous metabolism, which may lead to bone mineralization defects [26, 54]. The cell proliferation and osteogenic differentiation of hBMSCs cultured in 2Mg-TCP group (initial Mg^{2+} concentration was 5.25 ± 0.11 mM) and 4Mg-TCP (initial Mg^{2+}

concentration was 6.46 ± 0.19 mM) group were worse than those of 1Mg-TCP, which is consistent with the literature reports.

Although Mg^{2+} at concentrations below 10 mM has been reported to have no adverse effects on endothelial cells, some studies have reported that the viability of the endothelial cell tended to decrease with an increase in the Mg^{2+} concentration up to 12 mM, and the viability was highest at a low Mg^{2+} concentrations (approximately 2 mM) [55, 56]. Our experimental results on endothelial cells confirmed this, and HUVECs cultured in the 1Mg-TCP group (initial Mg^{2+} concentration of 2.31 ± 0.12 mM) proliferated faster than the other three groups did. The proliferation plateau of cells cultured in the 2Mg-TCP group and the inhibition of proliferation in the cells cultured in the 4Mg-TCP group may be caused by a decrease in cell viability. Differences in angiogenesis-related genes in HUVECs induced by four groups of Mg-TCP extracts may also be associated with decreased cell viability caused by high concentrations of Mg^{2+}. The relationship between the expression of angiogenesis-related genes of endothelial cells and the concentration of Mg^{2+} is rarely reported in the literature. Our research team will explore this further in the future.

Interestingly, the concentration of Ca^{2+} and Mg^{2+} in the extract decreased after the cells were cultured (Fig. 4). We speculate that there is a possible mechanism: dissolved mineral ions induce extracellular matrix mineralization and bioapatite deposition. Comparing the ICP-AES results, it can be seen that the concentration of mineral ions (Mg^{2+}, Ca^{2+}) slightly decreased after induction culture. This is most likely due to the formation of calcified nodules that cause the ions to deposit which was confirmed by ARS staining and quantification results (Fig. 8). Low concentrations of Mg^{2+} (1Mg-TCP group) significantly promoted the formation of calcium nodules during extracellular matrix mineralization. In addition, calcium phosphate materials can also absorb mineral ions and promote apatite deposition. [57, 58].

Acknowledgement This study was supported by the Science and Technology Planning Project of Guangdong Province of China under Grant No. 2017B090912007.

Compliance with ethical standards

Conflict of interest There is no conflict of interest in this manuscript.

Ethical statement There are no human or animal experiments carried out for this article.

References

1. de Sousa CA, Lemos CAA, Santiago-Júnior JF, Faverani LP, Pellizzer EP. Bone augmentation using autogenous bone versus biomaterial in the posterior region of atrophic mandibles: a systematic review and meta-analysis. J Dent. 2018;76:1–8.
2. Al-Nawas B, Schiegnitz E. Augmentation procedures using bone substitute materials or autogenous bone—a systematic review and meta-analysis. Eur J Oral Implantol. 2014;7:S219–34.
3. Barone A, Ricci M, Mangano F, Covani U. Morbidity associated with iliac crest harvesting in the treatment of maxillary and mandibular atrophies: a 10-year analysis. J Oral Maxillofac Surg. 2011;69:2298–304.
4. Calori GM, Colombo M, Mazza EL, Mazzola S, Malagoli E, Mineo GV. Incidence of donor site morbidity following harvesting from iliac crest or RIA graft. Injury. 2014;45:S116–20.
5. Šponer P, Kučera T, Brtková J, Urban K, Kočí Z, Měřička P, et al. Comparative study on the application of mesenchymal stromal cells combined with tricalcium phosphate scaffold into femoral bone defects. Cell Transplant. 2018;27:1459–68.
6. Agarwal R, García AJ. Biomaterial strategies for engineering implants for enhanced osseointegration and bone repair. Adv Drug Deliv Rev. 2015;94:53–62.
7. Chia HN, Wu BM. Recent advances in 3D printing of biomaterials. J Biol Eng. 2015;9:4.
8. Zou F, Zhao N, Fu X, Diao J, Ma Y, Cao X, et al. Enhanced osteogenic differentiation and biomineralization in mouse mesenchymal stromal cells on a β-TCP robocast scaffold modified with collagen nanofibers. RSC Adv. 2016;6:23588–98.
9. Ke D, Bose S. Doped tricalcium phosphate bone tissue engineering scaffolds using sucrose as template and microwave sintering: enhancement of mechanical and biological properties. Mater Sci Eng C Mater Biol Appl. 2017;78:398–404.
10. Sariibrahimoglu K, Wolke JG, Leeuwenburgh SC, Yubao L, Jansen JA. Injectable biphasic calcium phosphate cements as a potential bone substitute. J Biomed Mater Res B Appl Biomater. 2014;102:415–22.
11. Gleadall A, Visscher D, Yang J, Thomas D, Segal J. Review of additive manufactured tissue engineering scaffolds: relationship between geometry and performance. Burns Trauma. 2018;6:19.
12. Zhang L, Yang G, Johnson BN, Jia X. Three-dimensional (3D) printed scaffold and material selection for bone repair. Acta Biomater. 2019;84:16–33.
13. Lai Y, Cao H, Wang X, Chen S, Zhang M, Wang N, et al. Porous composite scaffold incorporating osteogenic phytomolecule icariin for promoting skeletal regeneration in challenging osteonecrotic bone in rabbits. Biomaterials. 2018;153:1–13.
14. Kim SE, Shim KM, Jang K, Shim JH, Kang SS. Three-dimensional printing-based reconstruction of a maxillary bone defect in a dog following tumor removal. In Vivo. 2018;32:63–70.
15. Bose S, Banerjee D, Robertson S, Vahabzadeh S. Enhanced in vivo bone and blood vessel formation by iron oxide and silica doped 3D printed tricalcium phosphate scaffolds. Ann Biomed Eng. 2018;46:1241–53.
16. Diao J, OuYang J, Deng T, Liu X, Feng Y, Zhao N, et al. 3D-plotted beta-tricalcium phosphate scaffolds with smaller pore sizes improve *in vivo* bone regeneration and biomechanical properties in a critical-sized calvarial defect rat model. Adv Healthc Mater. 2018;7:e1800441.
17. Fielding G, Bose S. SiO_2 and ZnO dopants in three-dimensionally printed tricalcium phosphate bone tissue engineering scaffolds enhance osteogenesis and angiogenesis *in vivo*. Acta Biomater. 2013;9:9137–48.
18. Sader MS, Martins VCA, Gomez S, LeGeros RZ, Soares GA. Production and in vitro characterization of 3D porous scaffolds

made of magnesium carbonate apatite (MCA)/anionic collagen using a biomimetic approach. Mater Sci Eng C Mater Biol Appl. 2013;33:4188–96.
19. Wang W, Yeung KWK. Bone grafts and biomaterials substitutes for bone defect repair: A review. Bioact Mater. 2017;2:224–47.
20. Tarafder S, Dernell WS, Bandyopadhyay A, Bose S. SrO- and MgO-doped microwave sintered 3D printed tricalcium phosphate scaffolds: mechanical properties and *in vivo* osteogenesis in a rabbit model: SrO- and MgO-doped microwave sintered 3D printed tricalcium phosphate scaffolds. J Biomed Mater Res B Appl Biomater. 2015;103:679–90.
21. Cooke JP, Losordo DW. Nitric oxide and angiogenesis. Circulation. 2002;105:2133–5.
22. Romani AMP. Beneficial role of Mg^{2+} in prevention and treatment of hypertension. Int J Hypertens. 2018;2018:9013721.
23. Richard RC, Sader MS, Dai J, Thiré RM, Soares GD. Beta-type calcium phosphates with and without magnesium: From hydrolysis of brushite powder to robocasting of periodic scaffolds. J Biomed Mater Res A. 2014;102:3685–92.
24. Sa MW, Nguyen BB, Moriarty RA, Kamalitdinov T, Fisher JP, Kim JY. Fabrication and evaluation of 3D printed BCP scaffolds reinforced with ZrO_2 for bone tissue applications. Biotechnol Bioeng. 2018;115:989–99.
25. Hussain A, Bessho K, Takahashi K, Tabata Y. Magnesium calcium phosphate/β -tricalcium phosphate incorporation into gelatin scaffold: an in vitro comparative study: MCP/β TCP gelatin scaffolds: comparative study. J Tissue Eng Regen Med. 2014;8:919–24.
26. Singh SS, Roy A, Lee B, Banerjee I, Kumta PN. Synthesis, characterization, and in vitro cytocompatibility of amorphous β-tri-calcium magnesium phosphate ceramics. Mater Sci Eng C Mater Biol Appl. 2016;67:636–45.
27. Yu Y, Xu C, Dai H. Preparation and characterization of a degradable magnesium phosphate bone cement. Regen Biomater. 2016;3:231–7.
28. Famery R, Richard N, Boch P. Preparation of α- and β-tricalcium phosphate ceramics, with and without magnesium addition. Ceram Int. 1994;20:327–36.
29. Xiao J, Yang S. Bio-inspired synthesis: understanding and exploitation of the crystallization process from amorphous precursors. Nanoscale. 2012;4:54–65.
30. Kang Y, Kim S, Fahrenholtz M, Khademhosseini A, Yang Y. Osteogenic and angiogenic potentials of monocultured and co-cultured human-bone-marrow-derived mesenchymal stem cells and human-umbilical-vein endothelial cells on three-dimensional porous beta-tricalcium phosphate scaffold. Acta Biomater. 2013;9:4906–15.
31. Komori T. Roles of Runx2 in skeletal development. In: Groner Y, Ito Y, Liu P, Neil JC, Speck NA, van Wijnen A, editors. RUNX Proteins in Development and Cancer. Advances in Experimental Medicine and Biology, vol 962. Singapore: Springer; 2017. p. 83–93.
32. Haq F, Ahmed N, Qasim M. Comparative genomic analysis of collagen gene diversity. 3 Biotech. 2019;9:83.
33. Gordon JA, Tye CE, Sampaio AV, Underhill TM, Hunter GK, Goldberg HA. Bone sialoprotein expression enhances osteoblast differentiation and matrix mineralization in vitro. Bone. 2007;41:462–73.
34. Siragusa M, Fleming I. The eNOS signalosome and its link to endothelial dysfunction. Pflugers Arch. 2016;468:1125–37.
35. Palaveniene A, Tamburaci S, Kimna C, Glambaite K, Baniukaitiene O, Tihminlioğlu F, et al. Osteoconductive 3D porous composite scaffold from regenerated cellulose and cuttlebone-derived hydroxyapatite. J Biomater Appl. 2019;33:876–90.
36. Guo Y, Tran RT, Xie D, Wang Y, Nguyen DY, Gerhard E, et al. Citrate-based biphasic scaffolds for the repair of large segmental bone defects: citrate-based biphasic scaffolds. J Biomed Mater Res A. 2015;103:772–81.
37. Anandan D, Mary Stella S, Arunai Nambiraj N, Vijayalakshmi U, Jaiswal AK. Development of mechanically compliant 3D composite scaffolds for bone tissue engineering applications. J Biomed Mater Res A. 2018;106:3267–74.
38. Nabiyouni M, Ren Y, Bhaduri SB. Magnesium substitution in the structure of orthopedic nanoparticles: A comparison between amorphous magnesium phosphates, calcium magnesium phosphates, and hydroxyapatites. Mater Sci Eng C Mater Biol Appl. 2015;52:11–7.
39. Frasnelli M, Sglavo VM. Effect of Mg^{2+} doping on beta–alpha phase transition in tricalcium phosphate (TCP) bioceramics. Acta Biomater. 2016;33:283–9.
40. Frasnelli M, Sglavo VM. Alpha-beta phase transformation in tricalcium phosphate (TCP)ceramics: effect of Mg^{2+} doping. In: Narayan RJ, Colombo P, editors. Ceramic engineering and science proceedings. Hoboken: Wiley; 2015. p. 63–70.
41. Zhang K, Lin S, Feng Q, Dong C, Yang Y, Li G, et al. Nanocomposite hydrogels stabilized by self-assembled multivalent bisphosphonate-magnesium nanoparticles mediate sustained release of magnesium ion and promote in situ bone regeneration. Acta Biomater. 2017;64:389–400.
42. Cipriano AF, Lin J, Miller C, Lin A, Cortez Alcaraz MC, Soria P, et al. Anodization of magnesium for biomedical applications—Processing, characterization, degradation and cytocompatibility. Acta Biomater. 2017;62:397–417.
43. Yu Y, Jin G, Xue Y, Wang D, Liu X, Sun J. Multifunctions of dual Zn/Mg ion co-implanted titanium on osteogenesis, angiogenesis and bacteria inhibition for dental implants. Acta Biomater. 2017;49:590–603.
44. Wang J, Ma XY, Feng YF, Ma ZS, Ma TC, Zhang Y, et al. Magnesium ions promote the biological behaviour of rat calvarial osteoblasts by activating the PI3K/Akt signalling pathway. Biol Trace Elem Res. 2017;179:284–93.
45. Zhang X, Zu H, Zhao D, Yang K, Tian S, Yu X, et al. Ion channel functional protein kinase TRPM7 regulates Mg ions to promote the osteoinduction of human osteoblast via PI3K pathway: In vitro simulation of the bone-repairing effect of Mg-based alloy implant. Acta Biomater. 2017;63:369–82.
46. Gu YX, Du J, Si MS, Mo JJ, Qiao SC, Lai HC. The roles of PI3K/Akt signaling pathway in regulating MC3T3-E1 preosteoblast proliferation and differentiation on SLA and SLActive titanium surfaces. J Biomed Mater Res A. 2013;101:748–54.
47. Zhang J, Ma X, Lin D, Shi H, Yuan Y, Tang W, et al. Magnesium modification of a calcium phosphate cement alters bone marrow stromal cell behavior via an integrin-mediated mechanism. Biomaterials. 2015;53:251–64.
48. Lapidos KA, Woodhouse EC, Kohn EC, Masiero L. $Mg^{(++)}$-induced endothelial cell migration: substratum selectivity and receptor-involvement. Angiogenesis. 2001;4:21–8.
49. Meng N, Han L, Pan X, Su L, Jiang Z, Lin Z, et al. Nano-$Mg(OH)^2$-induced proliferation inhibition and dysfunction of human umbilical vein vascular endothelial cells through caveolin-1-mediated endocytosis. Cell Biol Toxicol. 2015;31:15–27.
50. Yoshizawa S, Brown A, Barchowsky A, Sfeir C. Magnesium ion stimulation of bone marrow stromal cells enhances osteogenic activity, simulating the effect of magnesium alloy degradation. Acta Biomater. 2014;10:2834–42.
51. Su ZX, Shi YQ, Lu ZY, Li RL, Wang XL, Ning BB, et al. Comparative study of nanostructured carriers of calcium phosphate and magnesium phosphate loaded with SRT1720 for the protection of H_2O_2-induced senescent endothelium. Am J Transl Res. 2018;10:2068–77.

52. Zhao N, Zhu D. Endothelial responses of magnesium and other alloying elements in magnesium-based stent materials. Metallomics. 2015;7:118–28.
53. Wong HM, Wu S, Chu PK, Cheng SH, Luk KD, Cheung KM, et al. Low-modulus Mg/PCL hybrid bone substitute for osteoporotic fracture fixation. Biomaterials. 2013;34:7016–32.
54. Lin Z, Wu J, Qiao W, Zhao Y, Wong KHM, Chu PK, et al. Precisely controlled delivery of magnesium ions thru sponge-like monodisperse PLGA/nano-MgO-alginate core-shell microsphere device to enable in situ bone regeneration. Biomaterials. 2018;174:1–16.
55. Mochizuki A, Yahata C, Takai H. Cytocompatibility of magnesium and AZ31 alloy with three types of cell lines using a direct in vitro method. J Mater Sci Mater Med. 2016;27:145.
56. Cipriano AF, Sallee A, Tayoba M, Cortez Alcaraz MC, Lin A, Guan RG, et al. Cytocompatibility and early inflammatory response of human endothelial cells in direct culture with Mg–Zn–Sr alloys. Acta Biomater. 2017;48:499–520.
57. Belcarz A, Zalewska J, Pałka K, Hajnos M, Ginalska G. Do Ca^{2+}-adsorbing ceramics reduce the release of calcium ions from gypsum-based biomaterials? Mater Sci Eng C Mater Biol Appl. 2015;47:256–65.
58. Schamel M, Barralet JE, Groll J, Gbureck U. In vitro ion adsorption and cytocompatibility of dicalcium phosphate ceramics. Biomater Res. 2017;21:10.